Energieforschungsprogramm

Publizierbarer Endbericht

Programmsteuerung:
Klima- und Energiefonds

Programmabwicklung:
Österreichische Forschungsförderungsgesellschaft mbH (FFG)

Endbericht
erstellt am
20/05/2019

Projekttitel: PERMASOL

Projektnummer: 848929

Ausschreibung	1. Ausschreibung Energieforschungsprogramm
Projektstart	01/09/2015
Projektende	31/12/2018
Gesamtprojektdauer (in Monaten)	40 Monate
ProjektnehmerIn (Institution)	AIT Austrian Institute of Technology
AnsprechpartnerIn	Dr. Theodoros Dimopoulos
Postadresse	Giefinggasse 4, 1210 Vienna
Telefon	050 550 6201
Fax	050 550 6311
E-mail	Theodoros.dimopoulos@ait.ac.at
Website	www.ait.ac.at

PERMASOL

Perovskite Materials for Efficient Solar Cells

AutorInnen:
Dr. Theodoros Dimopoulos (AIT)
Dr. Gregor Trimmel (TU Graz)
Dr. Bernhard Lamprecht (Joanneum Research)
Dr. Iosif Galanakis (University of Patras)

1 Contents

2 Introduction

2.1 Focus and tasks

The focus of PERMASOL was the investigation of lead (Pb)-free perovskite materials for use as efficient and stable light absorbers in photovoltaic (PV) solar cells. These materials could potentially replace the currently used Pb (lead)-based solar absorber, the toxicity of which is an obstacle for the large-scale commercialization of this very promising PV technology.

At the start of the PERMASOL project, only a few Pb-free perovskite absorbers had been investigated in the literature. The limited existing knowledge on Pb-free alternatives demanded that the project implements **electronic band structure simulation methods** (realized by the **University of Patras**, Greece) to enable screening as many candidates as possible, before moving to the **investigation of the most promising Pb-free perovskites in the laboratory (AIT, ICTM, JR)**.
The absorber materials which experimentally showed suitable properties (bandgap, processability, stability, etc) were finally **implemented into solar cells (AIT, ICTM, JR)**. In certain cases, it was even possible to apply a **low-temperature approach** to process the complete solar cell (one that is similar to organic photovoltaics). Low temperature processing has a particular advantage when it comes to the future industrial up-scaling, ease of production and application of flexible substrates for roll-to-roll processing. To enable low-temperature processing, also other material components needed to be developed, like **electron and hole transport layers**, which were tested and evaluated with respect to their compatibility with the new perovskite absorbers.
Despite the above, certain Pb-free perovskite absorbes were clearly more efficient when implemented into a high-temperature cell architecture (with certain layers, such as mesoporous titanium oxide) being processed at excess of 400°C. We have also investigated this architecture, as our primary focus was to demonstrate the potential of the Pb-free perovskite absorbers.
Finally, it was imperative to employ **elaborate characterization techniques**, such as time-dependent photoluminescence, to investigate the photo-generated carrier transport in these newly developed materials, integrated into the different solar cell architectures.

Reflecting the abovementioned targets and tasks, the project was separated into the following workpackeges (WP):

Work-packages
WP1: Project management and dissemination
WP2: Simulation and design of materials
WP3: Synthesis and characterization of materials
WP4: Investigation of the charge carrier transport mechanisms
WP5: Fabrication and characterization of perovskite solar cells

2.2 Integration into the programme

The project was integrated in the **priority topic** (Themenfeld 1): **Emerging Technologies** of the "Energieforschung" Programme of the KLIEN, with focus: development of new materials (Werkstoff- und Materialforschung, mit Bezug auf die Entwicklung neuer Materialien).
Indeed PERMASOL dealt with application-oriented materials research for the development of novel, environment-friendly, Pb-free perovskite absorbers, in order to enable solar power generation at low cost and high efficiency.
Programme objectives: PERMASOL met all three of the programme objectives.

The **objective 1**: "Contribution to the fulfillment of the energy, climate and climate change technological policy requirements of the Austrian federal government" is addressed by achieving an effective cost reduction of future thin film photovoltaic technologies. Both through the saving of raw materials and through improved production processes, the planned new development will make a contribution to increasing the share of PV and thus to increasing the share of renewable energies in the energy mix. In line with the Austrian Energy Strategy, the project thus contributes to the reduction of CO_2 emissions from fossil sources and supports Austria's desire for independence from imported energy and an increase in the quality of life.

The targeted low cost and expected high energy yield of the proposed technology are also in line with **Objective 2**: "Increase the affordability of sustainable energy and innovative energy technologies". Improved processes, increase in affordability and innovative structures will facilitate rapid market genetration and the technology already in place give new impetus to interested national companies.

Finally, the planned project also contributes to **Objective 3** "Establishing and safeguarding technological leadership and strengthening the international competitiveness of Austrian companies", specifically in the field of thin-film photovoltaics. The technological approaches addressed in the proposed project can be used by companies in the sector solar cell manufacturing, development of coating tools or building integration of PV, bringing important competitive advantages. From this point of view, the project can make a significant contribution to strengthening Austria as an innovation location.

3 Results

Below we will give a summary of the most important results of the project, focusing on the various Pb-free perovskite absorbers investigated and their integration into solar cells. We will start with the energy band structure simulations and then we will proceed with the presentation of the experimental results.

3.1 Energy band structure simulations of Pb-free perovskites

[For more details see ref. [1–3] and references therein]

Our target was to identify new hybrid halide perovskites, which could substitute the methylammonium (MA)-lead-iodide ($MAPbI_3$), which was the state-of-the-art efficient perovskite absorber when the project commenced. To reach our target we have studied, using ab-initio electronic structure calculations, the properties of $MABX_3$ compounds with the divalent cation B being one of the Ca, Sr, Ba, Zn, Cd, Hg, Ge, Sn or Pb atoms and considered all possible halogen atoms X = F,Cl, Br and I.
The first step was to use the VASP ab-initio technique in combination with the so-called PBEsol functional for the exchange-correlation to determine the equilibrium lattice constants for all 36 compounds, which allow the MA cation to relax within the cubic unit cell (Figure 1). We then employed the more sophisticated hybrid HSE06 and mBJ+PBEsol functionals to calculate the electronic properties of these compounds at the equilibrium and to extract the energy band gap. The simulations have shown that both lattice constants and energy gaps vary greatly depending on the choice for the divalent cation and the halogen atom.

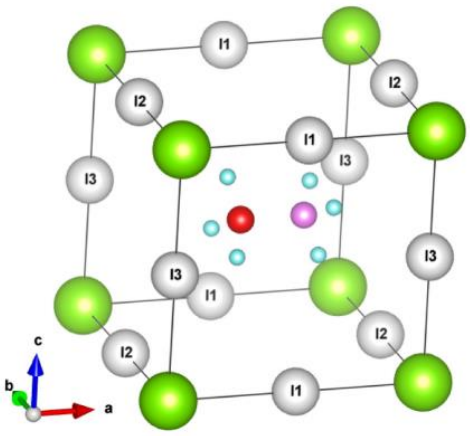

Figure 1. Cubic unit cell of the $MABI_3$ compounds. The divalent cations B (green spheres) are at the corners of the cube surrounded by six halogen atoms (gray atoms). There are three inequivalent halogen atoms in the unit cell at the midpoints of the edges. The C-N bond of the MA cation (CH_3NH_3) is along the x-axis, and each one of the C (red sphere) and N (purple sphere) atoms is surrounded by three H atoms (light blue spheres). We also denote the Cartesian axis x; y and z using the unit vectors **a**; **b** and **c**, respectively. (Figure from [1])

Tables 1, 2 and 3 summarize respectively the calculated lattice constants for the simulated compounds, the bandgap values for the compounds with a single halide perovskites and the bandgap values for the mixed halide perovskites.

$a_{eq}^{MABX_3}$ (Å)	X = F	X = Cl	X = Br	X = I
B = Ca	4.7059	5.4883	5.7590	6.1709
B = Sr	4.8907	5.7103	5.9886	6.4127
B = Ba	5.1694	6.0142	6.3127	6.7362
B = Zn	4.4958	5.1723	5.4276	5.8133
B = Cd	4.6656	5.3548	5.6088	5.9923
B = Hg	4.7385	5.4047	5.6563	6.0203
B = Ge	4.6771	5.3679	5.6023	5.9499
B = Sn	4.8581	5.6047	5.8431	6.2021
B = Pb	4.9354	5.7006	5.9454	6.3134

Table 1. Calculated equilibrium lattice constants, α_{eq}, in Å, for the hybrid halide perovskites using the PBEsol approximation. These perovskites have the chemical formula $MABX_3$. (Table from [1])

$MABX_3$	Band gap (eV) HSE06 [mBJ+PBEsol] (PBEsol)			
	X = F	X = Cl	X = Br	X = I
B = Ca	7.71[7.30](6.20)	6.30[5.20](4.80)	5.36[4.63](4.30)	4.00[3.57](3.40)
B = Sr	7.57[7.28](5.92)	6.30[5.70](4.92)	5.26[5.08](4.15)	4.23[4.00](3.52)
B = Ba	6.91[6.53](5.33)	5.84[5.30](4.89)	5.02[4.64](4.26)	3.86[3.84](3.27)
B = Zn	3.78[3.35](1.96)	1.94[1.80](0.81)	0.71[0.84](0.12)	0.00[0.00](0.00)
B = Cd	4.47[4.05](2.90)	2.42[2.11](1.52)	1.30[1.21](0.57)	0.22[0.23](0.00)
B = Hg	1.84[1.62](0.70)	0.23[0.00](0.00)	0.00[0.00](0.00)	0.00[0.00](0.00)
B = Ge	4.12[3.33](2.66)	1.96[1.64](1.33)	1.51[1.37](1.07)	1.21[1.22](0.93)
B = Sn	3.61[3.07](2.24)	1.70[1.55](1.07)	1.19[1.10](0.84)	0.94[0.86](0.72)
B = Pb	4.78[4.16](3.28)	2.91[2.52](2.24)	2.44[2.28](1.73)	1.82[1.85](1.49)

Table 2. Calculated energy gap in eV using the HSE06, the mBJ+PBEsol [in braces], and PBEsol functionals (the latter in parentheses) for the $MABX_3$ hybrid halide perovskites. The zero values correspond to a gapless (zero-gap) semiconducting behavior. (Figure from [1])

	$MAGe(Cl_2I)$	$MAGe(I_2Cl)$		$MACa(Cl_2I)$	$MACa(I_2Cl)$
I-case	0.93	0.70	I-case	4.01	3.48
II-case	0.71	0.82	II-case	4.17	3.51
III-case	0.83	0.80	III-case	4.01	3.48
$MAGeCl_3$	1.58	1.82	$MACaCl_3$	4.75	4.25
$MAGeI_3$	0.69	0.81	$MACaI_3$	2.98	3.16
	$MAPb(Cl_2I)$	$MAPb(I_2Cl)$		$MABa(Cl_2I)$	$MABa(I_2Cl)$
I-case	1.41	1.51	I-case	4.04	3.66
II-case	1.52	1.40	II-case	4.00	3.65
III-case	1.61	1.30	III-case	4.04	3.62
$MAPbCl_3$	2.44	2.52	$MABaCl_3$	4.58	4.18
$MAPbI_3$	1.01	1.30	$MABaI_3$	3.34	3.26
	$MAPb(Cl_2Br)$	$MAPb(Br_2Cl)$		$MABa(Cl_2Br)$	$MABa(Br_2Cl)$
I-case	2.04	1.83	I-case	4.64	4.27
II-case	1.84	1.93	II-case	4.54	4.30
III-case	1.94	1.83	III-case	4.55	4.30
$MAPbCl_3$	2.25	2.44	$MABaCl_3$	4.69	4.67
$MAPbBr_3$	1.53	1.73	$MABaBr_3$	4.36	4.25

Table 3. Calculated energy gaps in eV using the PBEsol functional for the mixed hybrid halide perovskites. The terms ‘‘I, II and III” correspond to the position of the single halogen atom in the unit cell. We have also calculated the energy gaps for the perfect compounds (last two lines in each case) at the lattice constants of the mixed hybrid halide perovskites. (Figure from [1])

Compounds based on alkali earth atoms show very large band gaps, being transparent to light in the optical regime, while the compounds based on Zn, Cd and Hg show much smaller band gaps and some of them are even gapless semiconductors. Among them, $MAZnCl_3$ and $MACdBr_3$ are potential candidates to replace $MAPbI_3$. The Ge compounds seem to be very promising and, more especially, our calculations suggest that $MAGeCl_3$ and $MAGeBr_3$ are suitable to replace $MAPbI_3$ in devices. The width of the energy gaps depends on the kind of hybridization forming the gap. For the mixed hybrid halide perovskites (mixing two kind of halogen atoms), although we could tune the values for the energy band gaps, there is no simple pattern to predict the exact value based on the properties of the parent perfect compounds. Consequently, we conclude that it is possible to find lead-free perovskites that can be used in energy technology applications like solar cells and optoelectronics, though the properties are materials-specific and extended state-of-the-art, heavy ab-initio calculations are a prerequisite for any reliable result.

The investigation continued by expanding the work for Cs-based compounds having the chemical formula $CsBX_3$. First, we considered only the cubic structure, presented in **Figure 2**, considering all possible combinations of divalent cations and halogen anions, similarly to the $MABX_3$ compounds above. We then computed the equilibrium lattice constants and afterwards the electronic properties of these compounds, focusing on the width of the energy band gap. Second, we considered the experimental lattice structures for the $CsBX_3$ which have been grown successfully in literature reports and we have calculated the energy band gap also in their case. The latter crystallize not only in the cubic but also in orthorhombic lattices, since as it is well known perovskite materials undergo several structural transitions.

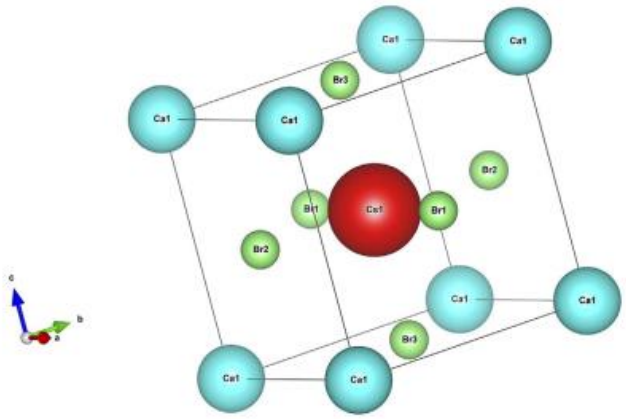

Figure 2. Schematic representation of the cubic lattice structure assumed for the $CsBX_3$ compounds. The Cs atom is at the center of the cube, the divalent B cations are at the corners of the cube, and the halogen atoms are at the center of the faces. (Figure from [2])

	Band gap (eV)			
	mBJ + PBEsol (PBEsol) [HSE06]			
$CsBX_3$	X = F	X = Cl	X = Br	X = I
B = Ca	1.62 (0.59)	0.94 (0.58)	0.95 (0.41)	0.60 (0.24)
B = Sr	2.51 (1.40)	1.87 (1.10)	1.59 (0.79)	1.29 (0.64)
B = Ba	3.30 (2.14)	2.66 (1.88)	2.40 (1.50)	1.26 (1.26)
B = Zn	0.46 (0.00)	0.13 (0.00)	0.27 (0.00)	0.36 (0.00)
B = Cd	0.21 (0.00)	0.00 (0.00)	0.09 (0.00)	0.09 (0.00)
B = Hg	0.00 (0.00)	0.00 (0.00)	0.00 (0.00)	0.00 (0.00)
B = Ge	0.79 (0.00)	0.40 (0.00)	0.52 (0.00)	0.28 (0.00)
B = Sn	0.75 (0.00)	0.47 (0.00)	0.46 (0.00)	0.45 (0.00)
B = Pb	0.82 (0.00)	0.45 (0.00)	0.53 (0.00) [0.49]	0.33 (0.00) [0.38]

Table 4. Calculated energy gaps in eV using the mBJ+PBEsol and PBEsol functionals (the latter in parentheses) for the cubic $CsBX_3$ halide perovskites. The zero values correspond to a gapless (zero-gap) semiconducting behavior. We also provide the HSE06 values in braces where available. (Figure from [2])

For the cubic halide perovskites, the band gap values are summarized in **Table 4.** To elucidate the trends observed in the calculated band gap energies, the atom- and orbital resolved DOS for the Cs(Zn, Ca, or Ge)Br_3 compounds using the mBJ+PBEsol functional, were calculated. In all three cases the valence bands are made up from the p states of the Br atoms, with a very small s admixture. In the case of CsGeBr3 the conduction band is made up from the Ge empty 4p states and thus the gap is due to the p–p hybridization. A similar situation occurs if instead of Ge we have the isovalent Sn or Pb. For Ca and the isovalent Sr and Ba atoms, the conduction band is made up from the unoccupied d-orbitals. Finally, when the cation is a transition metal atom Zn, Cd, or Hg, although the p–p hybridization opens a sizeable

gap, the location of the Zn, Cd, or Hg s-states within the gap leads to much smaller energy gap values and even to the observed gapless behavior. For the $CsPbBr_3$ and $CsPbI_3$ compounds, calculations performed using also the HSE06 functional gave similar values to the ones with the mBJ+PBEsol.

The calculated band gap deviates strongly from the experimental value for $CsPbI_3$ in Ref. [5], which is 1.73 eV. Ref. [5] reveals that the experimental lattice constant of 6.1769 Å which strongly deviates from the calculated 6.7103 Å. One could thus assume that the discrepancy stems from the difference in the lattice constants. To elucidate more, ab initio calculations were also done for other Cs-based halide perovskites grown and characterized experimentally, the lattice of which, as determined experimentally, are either cubic or orthorhombic. The compounds crystallizing in the cubic structure are $CsSnCl_3$, $CsPbCl_3$, $CsPbBr_3$, and $CsPbI_3$. The experimental lattice constants for the cubic compounds are about 0.5 Å smaller than the theoretical ones, underlining a strong deviation.
Thus, contrary to the MA-based halide perovskites, in the case of the Cs-based halide perovskites, PBEsol fails to reproduce accurately the lattice constants. The smaller lattice constants lead also to large deviations in the calculated band gaps. Our calculations suggest that the case of $CsBX_3$ halide perovskites, unlike other families of halide perovskites, is not trivial and discrepancies between theory and experiments as well as between various functionals occur. Thus, further investigation is needed to clarify these points and allow for a more accurate study of these materials in the future.

Searching for the other possible replacements for the iodine methylammonium lead perovskite, we extended the ab-initio study to perovskites with low-symmetry lattices like trigonal, hexagonal, orthorhombic or monoclinic, with the general chemical formula $A_3B_2X_9$, where A is a Cs, Rb, K or methylammonium (MA) monovalent cation, B is a Bi or Sb trivalent cation, and X is an I, Br or Cl monovalent anion. Due to the large number of possible low-symmetry structures we have included in our study compounds for which the lattice structure is known experimentally. Our results showed that the values of the energy band gaps vary greatly among the studied materials and thus $A_3B_2X_9$ perovskites can be promising for PV applications. All materials under study produced band gaps ranging between 1 and 3 eV, due to the p p hybridization responsible for the appearance of the gap, and thus either are at the optical regime or near it and can find applications in optoelectronic and solar cell applications. The hybrid functional produced larger band gaps as expected for the trigonal and hexagonal materials, but we could not get convergence for the lower-symmetry orthorhombic and monoclinic lattice structures.

3.2 Germanium-based perovskites

[For more details see ref. [6] and references therein]

Germanium perovskite solar cells were first reported in 2015 [7] $CsGeI_3$ based solar cells led to a power conversion efficiency (PCE) of 0.11%, while a PCE of 0.2% was obtained using $MAGeI_3$ as absorber layer. For $CsGeI_3$, a theoretically maximum PCE of 27.9% was calculated.[8] We took this as incentive to investigate the PV performance and the stability of germanium halide perovskites and found that by partly substituting iodide with bromide, the perovskite $MAGeX_3$ (X = I, Br) becomes less prone to degradation and also the PV performance is significantly improved.

The germanium halide perovskites were synthesized from GeI_2, MAI ad MABr, respectively. DMF was used as solvent for the precursor solution. The X-ray diffractograms (XRD) of the prepared perovskites are shown in **Figure 3A**. The main peaks of the simulated pattern for trigonal $MAGeI_3$ (based on data from [9]) match well with the measured diffraction peaks of the prepared thin films. It is visible in **Figure 3B** that the peaks shift to higher 2θ values with increasing bromide content indicating a contraction of the unit cell. However, from the diffraction data it can be concluded that there is no change in the crystal structure in the investigated series of samples up to a bromide content of 33%. The peak at ~18.6° (marked with an asterisk) is only present upon addition of bromide.

The optical band gaps, extracted from the absorption onset, range between 2.0 eV for $MAGeI_3$ and 2.1 eV for $MAGeI_2Br$ with a continuous hypsochromic shift of the absorption onset with increasing bromide content (**Figure 3C**).

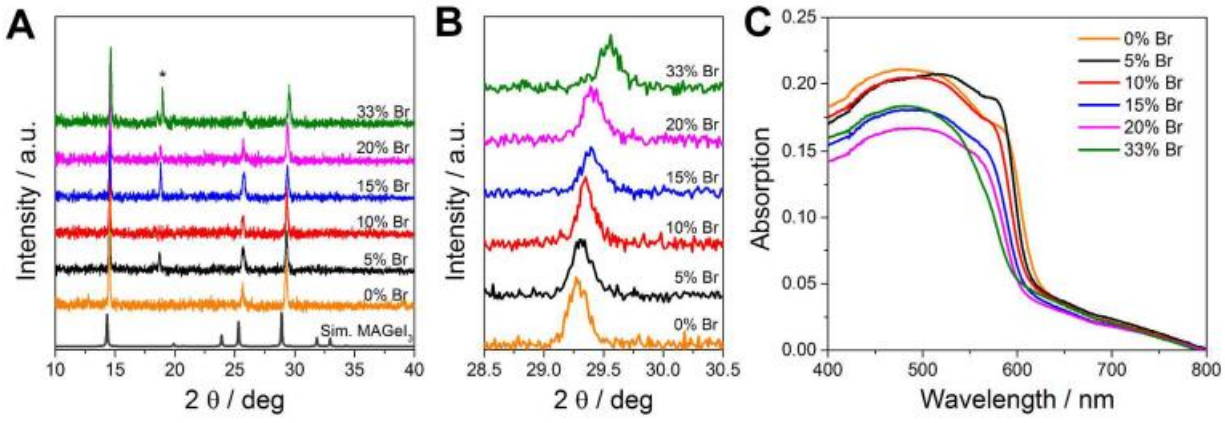

Figure 3. (A) XRD patterns of the mixed halide Ge perovskites with different Br-content and a simulated diffraction pattern for $MAGeI_3$, (B) magnification of the area between 28.5° and 30.5° 2θ, and (C) UV-Vis spectra of the prepared thin films. (Figure from [6])

The absorption data were used to evaluate the stability of the perovskite films under ambient conditions. The films were taken out of the nitrogen-filled glovebox and absorption spectra were

acquired over 24 h, while the films were exposed to ambient air. As shown in **Figure 4**, the absorption of the $MAGeI_3$ decreases much faster than the one of the $MAGeI_{2.7}Br_{0.3}$. For the latter, 65% of its initial absorption at 510 nm is retained, while for $MAGeI_3$ only 32%. This improved ambient stability of the Br-containing Ge perovskite correlates well with the lifetimes of the prepared solar cells.

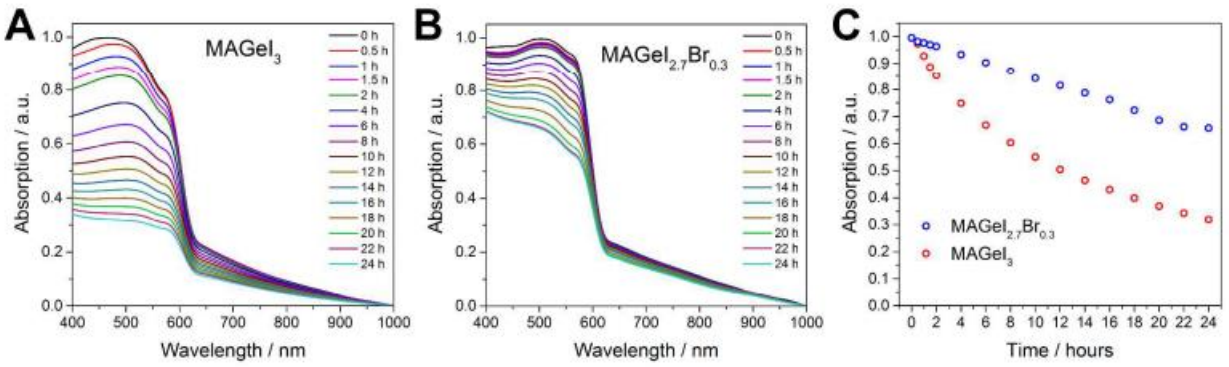

Figure 4. Time-resolved UV-Vis measurements to probe the ambient stability of the Ge perovskite samples (A: $MAGeI_3$;B: $MAGeI_{2.7}Br_{0.3}$) and the absorption intensity at 510 nm plotted vs. time (C). (Figure from [6])

To examine the PV properties of the perovskites, solar cells were prepared in the "organic" p-i-n solar cell architecture using PEDOT:PSS as hole transport layer (HTL) and $PC_{70}BM$ as electron transport layer (ETL). The results are summarized in **Figure 5**. Compared to [7], in which the $CsGeI_3$ and $MAGeI_3$-based solar cells have been prepared using mesoporous (mp) TiO_2 as ETL and spiro-OMeTAD as HTL, the open circuit voltage (V_{OC}) obtained for $MAGeI_3$-based solar cells in this work is considerably higher (345 mV compared to 150 mV). By fine-tuning the layers' thicknesses, the PCE of the $MAGeI_{2.7}Br_{0.3}$ solar cells could be further improved to 0.68% (measured without shadow mask). A measurement with a 2.9 x 2.9 mm² shadow mask led to a PCE of 0.57%. **Figure 6A** shows a cross section SEM image of this device. The different layers in the solar cell stack can be clearly recognized and appear very flat and homogenous.

The current density-voltage (J-V) curves measured in the dark and under 100 mW/cm² illumination are plotted in **Figure 6B**. The V_{OC} is 460 mV, the short circuit current density (J_{SC}) is 3.11 mA/cm² and the fill factor (FF) is 0.48, which results in a PCE of 0.68%. The series and shunt resistance of this solar cell are 30 Ω.cm² and 0.7 kΩ.cm², respectively. When measured with a shadow mask, the PCE decreases to 0.57%, which is based on a reduction of the J_{SC} to 2.43 mA/cm². The FF is slightly improves to 0.51 and the V_{OC} is unaffected by the illumination through the shadow mask. The maximum in the EQE spectrum is slightly below 500 nm, which is in good agreement with the absorption profile.

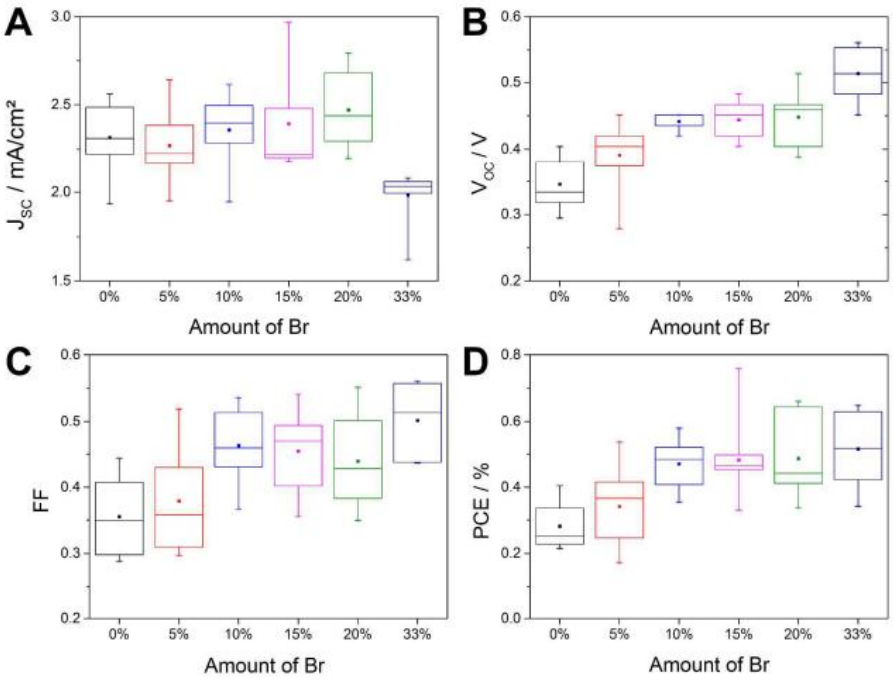

Figure 5. PV parameters (A: J_{SC} , B: V_{OC} , C: FF, and D: PCE) of the solar cells depending on the amount of Br as X-site anion in $MAGeX_3$ (X = I, Br). The best solar cells (minimum eight) of each absorber layer composition were considered for calculating the statistics. (Figure from [6])

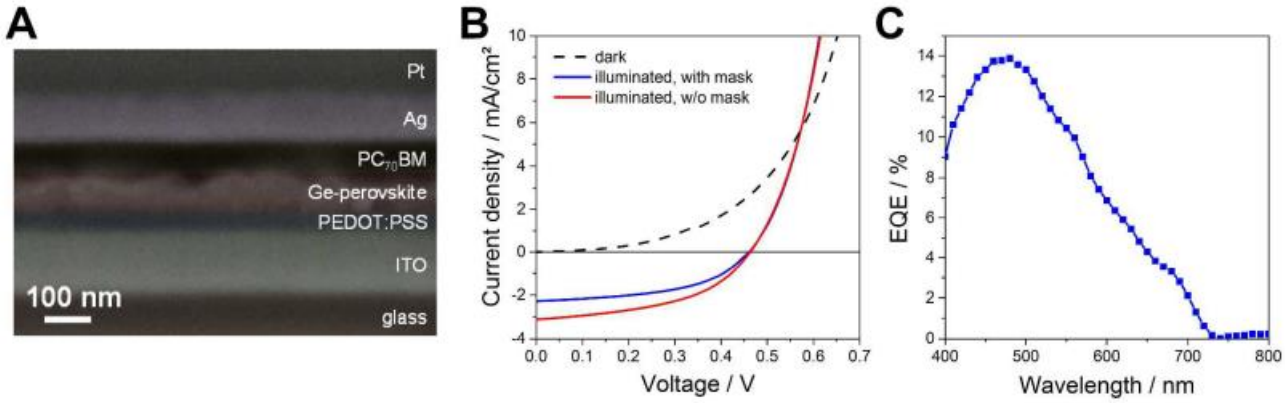

Figure 6. (A) Cross section SEM image of a solar cell, (B) J-V curves measured in the dark and under 100 mW/cm² illumination with and without 2.9 x 2.9 mm² shadow mask and (C) an EQE spectrum and of an optimized $MAGeI_{2.7}Br_{0.3}$ based solar cell. (Figure from [6])

3.3 Copper-based perovskites

2-dimensional, mixed halide perovskites: MA_2CuCl_4, MA_2CuCl_3Br, MA_2CuBr_3Cl, and $MA_2CuCl_{0.5}Br_{3.5}$ were synthesized from solutions containing DMF as solvent, in which $CuBr_2$, $CuCl_2$, MACl, MABr were dissolved in appropriate amounts to obtain various stoichiometries. The Cu perovskite could be processed on FTO, mp-TiO_2 and ZnO-nanorods (NRs) in the glovebox and demonstrated enhanced stability over several days in ambient conditions, even without encapsulation. This stability is attributed to its 2D structure which is resistant to the penetration of moisture.

Most interestingly, we have seen that with the inclusion of Br the films became darker (**Figure 7**) and the bandgap (as extracted from the transmittance spectra using Tauc plots) decreased from 2.84 eV for the case of pure MA_2CuCl_4 to 1.73 eV for $MA_2CuCl_{0.5}Br_{3.5}$ (**Figure 8**), which is within the values suitable for solar absorber. On the other hand, with the addition of Br, the solutions become harder to process into uniform films.

XRD measurements were realized to certify the presence of the Cu perovskite and were supported by crystal structure simulations. In order to obtain a reference pattern for the MA_2CuCl_4, the solution was firstly dried and then the powder was characterized by XRD. The obtained experimental peaks correspond to the simulated peaks for the 2D structure and the data from the literature [10]. No peaks belonging to MACl were resolved, meaning that practically all chemical reagents have reacted to form MA_2CuCl_4.

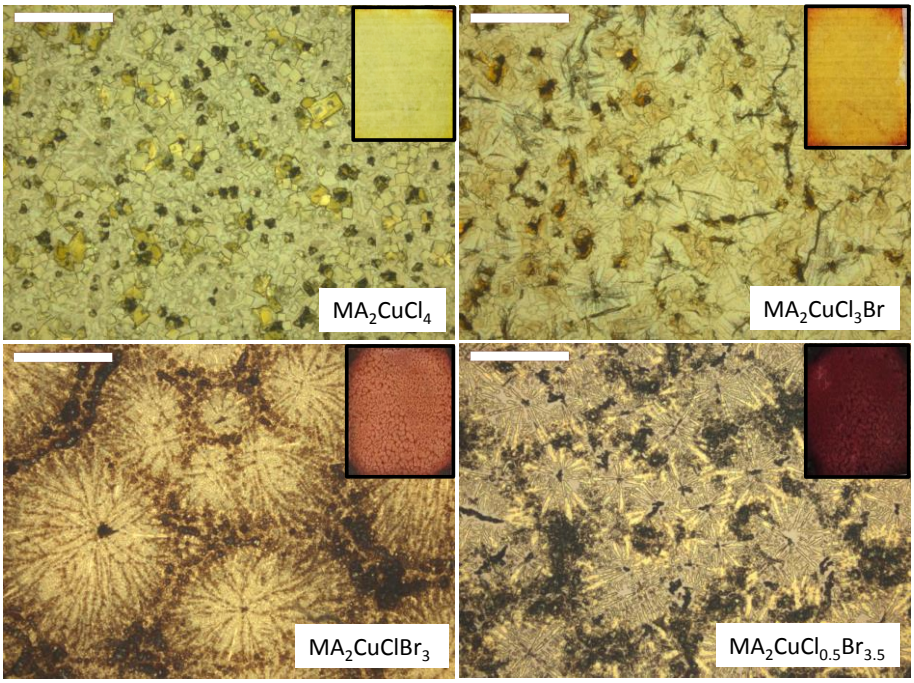

Figure 7: Optical microscopy images of 2D Cu mixed-halide perovskites (scale bar corresponds to 500 µm), together with photographs of the films (insets). The films are deposited on FTO-coated glass and have an estimated thickness of ~200 nm

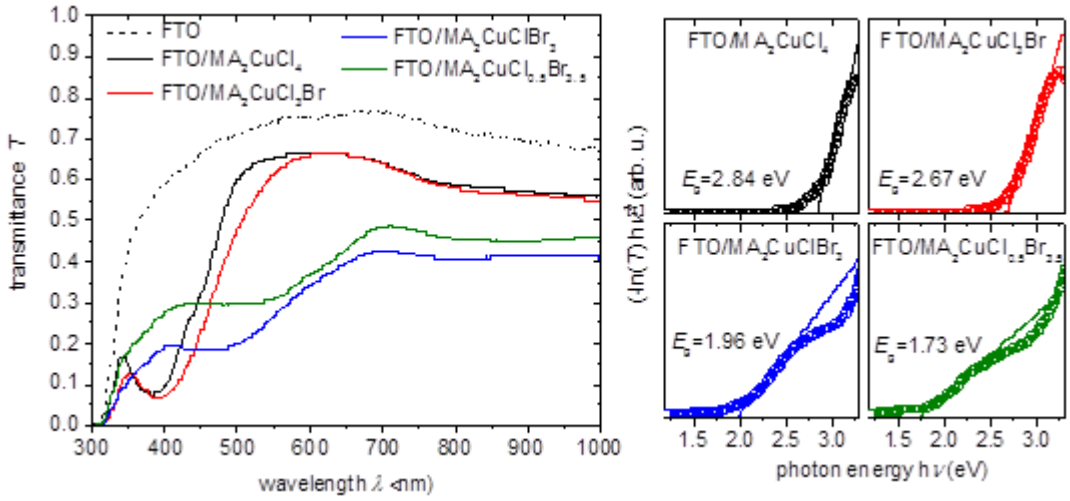

Figure 8: Transmittance spectra of the 2D Cu mixed-halide perovskites (and of the FTO reference) together with the corresponding Tauc plots, showing a decrease of the direct bandgap with the gradual addition of Br.

XRD of the films deposited on FTO-coated glass were acquired and shown in **Figure 9**. The MA_2CuCl_4 films (on FTO) glass show preferential growth with the dominant reflections coming from the (001), (002),…(00l) planes. No MACl peaks are observed. Further, the incorporation of bromine leads to the appearance of multiple crystalline phases, which can be attributed to the mixed halide phase of $MA_2CuCl_xBr_{4-x}$, but also to MA_2CuBr_4 and MA_2CuCl_4. The amount of the MA_2CuBr_4 increases with the increase of Br content. The reflections can be again assigned to the (00l) planes.

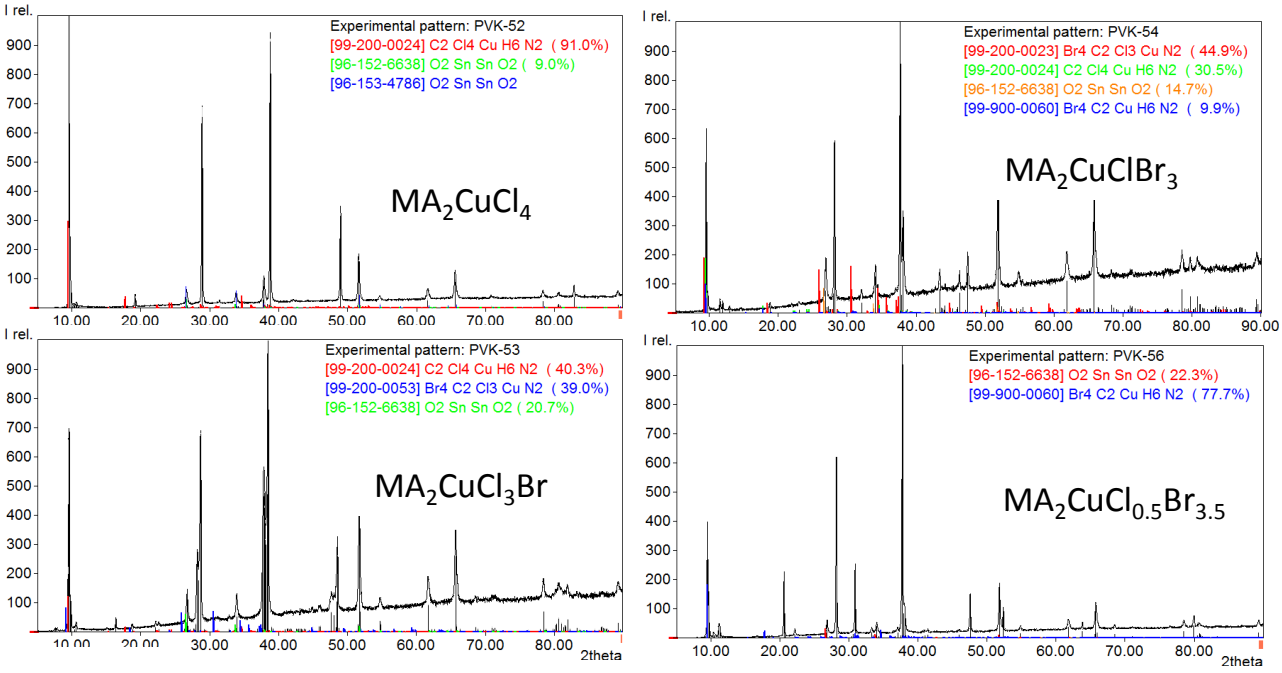

Figure 9: XRD measurements of the 2D Cu mixed halide perovskites.

Figure 10(a) shows the (001) peak for perovskite films with different Br content. The shift of the (001) peak to lower angles for increasing Br content is due to the lattice expansion due to the substitution of Cl- with Br- with larger ionic radius (181 pm vs 196 pm). The cross section SEM images show smooth

and compact layers of ~400 nm in thickness (**Figure 10(b) and 10(c)**). Plane view images show however that the layer is composed of platelets, at the junctions of which, holes reaching down to the substrate are present (**Figure 10(d) and (e)**). These holes would be detrimental for the solar cell operation. In the SEM image of **Figure 10(f)** we can see a delaminated piece of the layer where we can clearly distinguish the 2D planes that the layer is composed of.

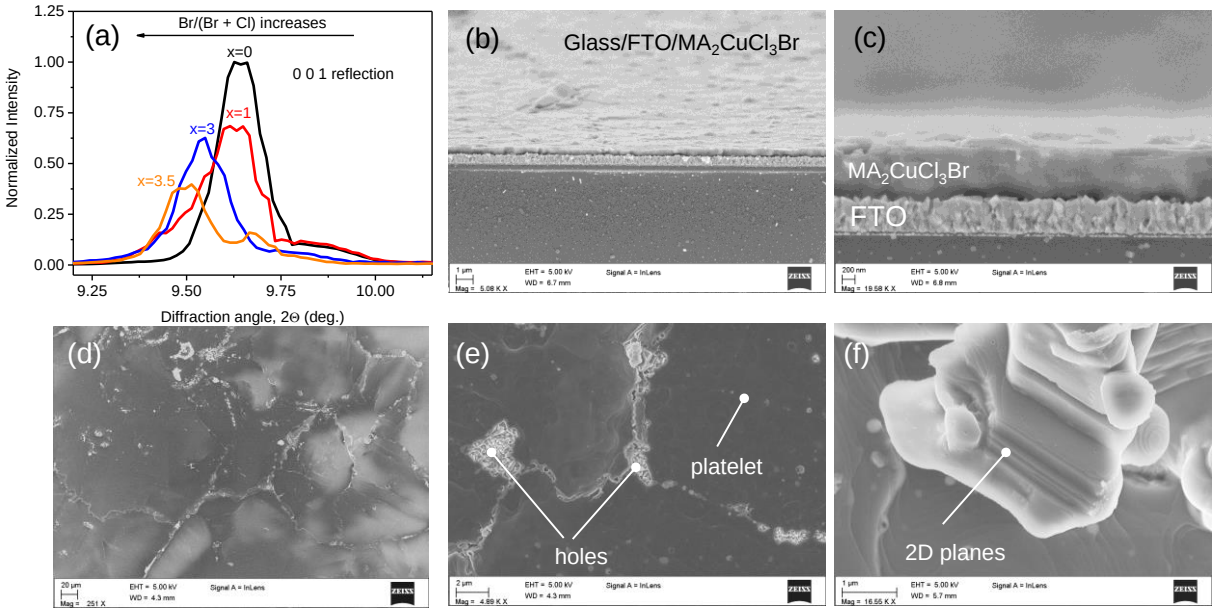

Figure 10. (a) The 001 XRD peak as it shifts to lower diffraction angles for increasing Br content. (b) an (c) cross section SEM images of the FTO/MA_2CuCl_3Br layers. (d) and (e) Plane view SEM images. (f) SEM images from a broken piece of the perovskite, showing that it is composed of flat planes.

Solar cells with the Cu perovskite absorber did not give PV performance. Nevertheless, Cu perovskites could be combined with Sn-perovskites to enhance the stability of the latter, as we will see in the last section.

3.4 Bismuth-based perovskites

[For more details see ref. [4] and references therein]

The novel A_6BX_9-type mixed-anion halogenobismuthate(III) semiconductor $(CH_3NH_3)_6BiI_{5.22}Cl_{3.78}$ (MBIC) was synthesized via a solution-based method from methylammonium iodide (CH_3NH_3I) and bismuth chloride ($BiCl_3$). Its structural, optical, and electrical properties were investigated in comparison to $(CH_3NH_3)_3Bi_2I_9$ (MBI) as reference compound. The structure of the compound is shown in **Figure 11**.

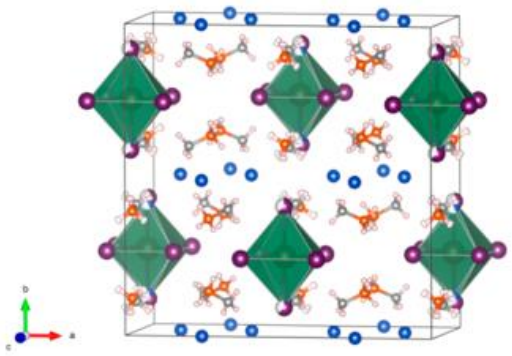

Figure 11. Crystal structure of MBIC at 100 K (space group: Cmma). BiX_6 octahedra are shown in green, with green spheres inside the polyhedra representing bismuth ions (Bi^{3+}), purple spheres iodide ions (I^-), blue spheres chloride ions (Cl^-), gray spheres nitrogen atoms, orange spheres carbon atoms, and white spheres hydrogen atoms. (Figure from [4])

XRD investigation (**Figure 12**) showed that the incorporation of Cl led to a notable change in the crystal structure compared to MBI. X-ray diffractograms for MBIC powder and thin film agree with the calculated powder XRD pattern using single crystal data. In thin MBIC films, a preferred orientation of the {0k0} planes parallel to the surface was found, which is also partially seen in the powder diffraction pattern because of the anisotropic shape of the crystals. This orientation effect is more pronounced in MBI thin films, with a preferential [00l] direction (along the c-axis). In addition, small intensity reflections in MBIC samples centered at 14.6° , 16.8° , 19.9° , 29.5° , 31.4° , 34.0° , and 37.8° are assigned to secondary MBI phase.

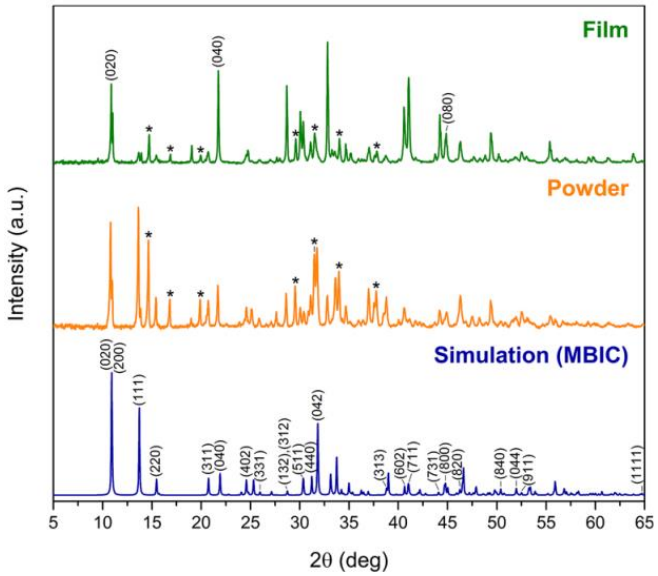

Figure 12. XRD patterns (Co K_α radiation, λ=1.79 Å) of a thin film (deposited on a glass substrate coated with mp-TiO_2) and a powder sample together with the simulated powder XRD pattern of MBIC including assignment of Miller indices (hkl) as deduced from the crystallographic data. Asterisks denote the presence of MBI as a secondary phase in the MBIC sample. (Figure from [4])

Figure 13 shows optical and scanning electron micrographs, supporting the strong orientation of the crystallites. Both compounds form hexagonally shaped platelets. **Figure 13B** shows SEM plane-view image of MBIC thin film on glass/c-TiO_2/mp-TiO_2 substrate. The image shows that the perovskite infiltrates the mp-TiO_2 and on the surface we find hexagonally shaped microcrystals or platelets with an average size of 2–3 μ m, as also see in optical light microscopy.

Both compounds exhibit a similar absorption behavior with a slight shift of the absorption onset for MBIC relative to MBI (**Figure 14**), which is associated with the additional contribution of chlorine p-states in the valence band of MBIC. Moreover, the absorption spectra of MBI and MBIC exhibit distinct absorption features. In the case of MBI, the first absorption band near the absorption edge was attributed to an intrinsic exciton band at 2.48 eV (499 nm). The exciton peak of MBIC at 475 nm is blue-shifted with respect to the peak position of MBI. The optical band gaps of thin films were extracted via the Tauc plot method, assuming in one case an indirect and in the other case a direct band transition. Satisfactory linear fits of the experimental data could be obtained for both cases, with similar extracted energy values. For MBI, a direct transition with an energy of 2.18 eV and an indirect one with 2.08 eV are extracted. For MBIC, the respective values are 2.38 eV (direct transition) and 2.25 eV (indirect transition); thus for both materials, the band gap is of an indirect nature.

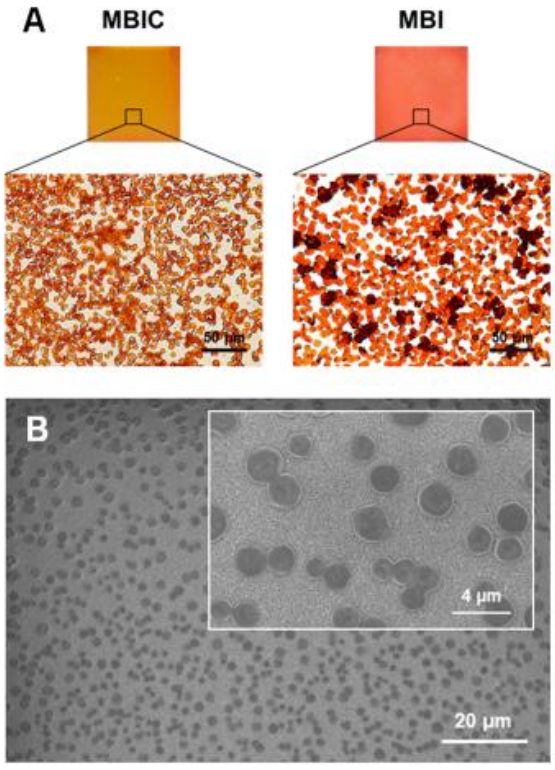

Figure 13. (A) Optical images of MBIC (left) and MBI (right) thin films (500-fold magnification) on microscope slides. (B) SEM top-view image of an MBIC film deposited on glass/c-TiO_2/mp-TiO_2. Inset shows the formation of hexagonally shaped platelets

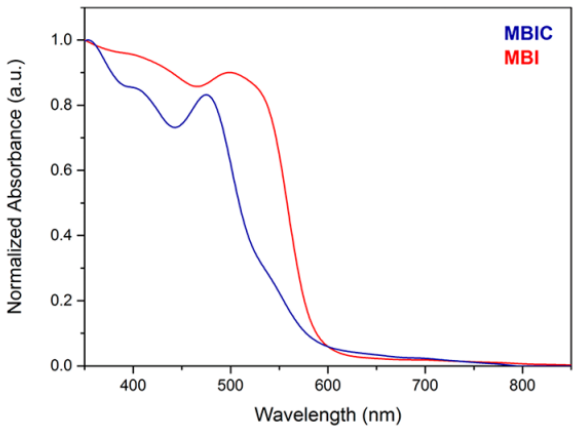

Figure 14. UV−vis absorption spectra of MBIC and MBI films. (Figure from [4])

or microcrystals and preferential orientation parallel to the substrate. (Figure from [4])

Furthermore, steady-state photoluminescence (PL) measurements were performed on MBI and MBIC thin films, which were excited with a laser. The emission properties of MBI and MBIC are quite similar, exhibiting a maximum between 515 and 530 nm as well as a broad, smaller shoulder around 650 nm. The emission peaks at about 650 nm can be associated with radiative recombination from intermediate band gap states corresponding to indirect band gap positions in the material. Further PL signals might arise from radiative recombination induced by additional trap states within the band gap resulting from the materials disorder. For ultrafast time-resolved photoluminescence (TRPL) measurements, MBIC and MBI thin films were prepared on glass and on mp-TiO_2 layers. The PL decay was modeled with a biexponential function consisting of a short-lived (τ_1) and a long-lived PL lifetime (τ_2) component. The PL intensity is dominated by the short-lifetime PL decay component with a fast initial drop (τ_1<1 ns), followed by a slower decay (τ_2 =3.0−4.6 ns). The average lifetimes τ on glass are 0.76 and 0.78 ns for MBIC and MBI, respectively. The PL decay times are reduced to 0.55 ns (for MBIC) and to 0.34 ns (for MBI) by introducing a mp-TiO_2 layer, suggesting that TiO2 is an effcient charge extraction layer.

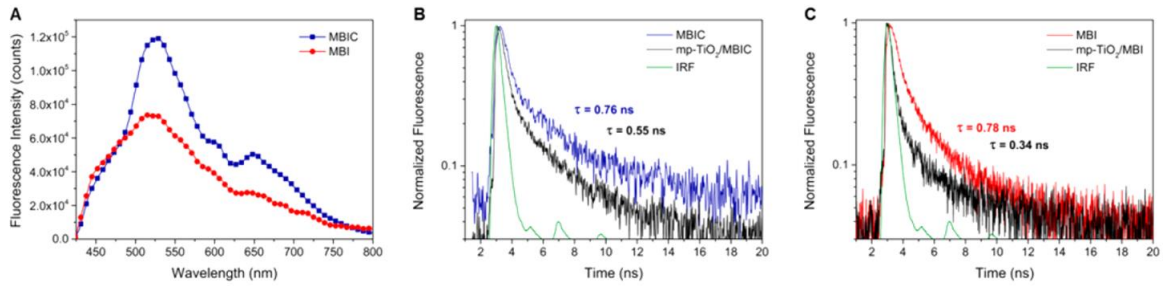

Figure 15. (A) Steady-state PL spectra of MBIC and MBI fi lms on glass (excitation wavelength: 405 nm). Time-resolved PL spectra of (B) MBIC fi lms and (C) MBI fi lms on glass and on mp-TiO_2 with the impulse response function (IRF) signal. (Figure from [4])

MBIC and MBI were implemented as absorbers in mesoscopic solar cells (ITO/c-TiO_2/mp-TiO_2/MBIC or MBI/spiro-OMeTAD/Au). A schematic representation of the energy level diagram and the device architecture are given in **Figure 16A,B**. **Figure 16C** shows the cross-section SEM image of the device. The MBIC absorber is infiltrated into the mp-TiO_2 scaffold, which has a layer thickness of about 350 nm.

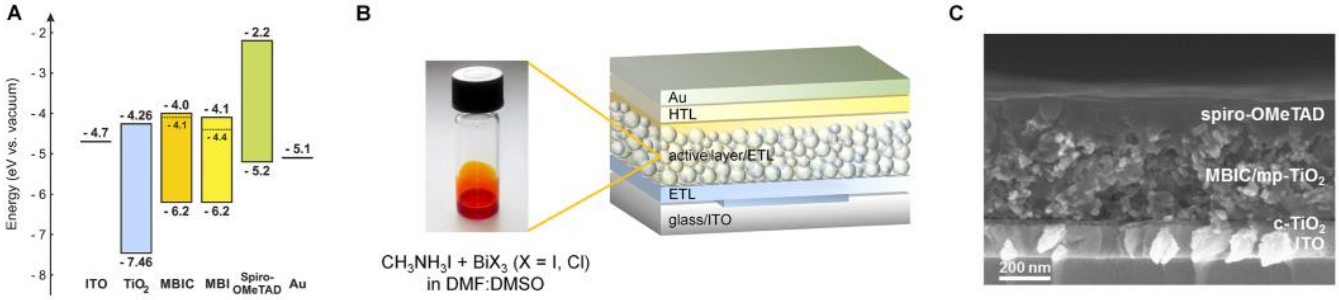

Figure 16. (A) Energy level diagram and (B) schematic representation of the PV cells. The VBM and Fermi energy level (dotted lines) of MBIC and MBI were determined by photoelectron spectroscopy. (C)

Cross- sectional SEM image of an MBIC-based mesoscopic solar cell. (Figure from [4])

J−V curves were recorded in both scan directions (**Figure 17A**), in the dark and under illumination (1000 W m^{-2}). The V_{OC} of the MBIC-based solar cells (ca. 0.45 V) are lower compared to the MBI-based devices (ca. 0.58 V), despite the fact that the band gap of MBIC is larger than that of MBI. The lower V_{OC} is in accordance with a less efficient electron extraction for MBIC, as derived from TRPL measurements. The higher J_{SC} of MBI compared to MBIC absorber layers can be explained by the broader absorption range and slightly lower optical band gaps of MBI. The PCE values of MBI-based solar cells (max. 0.26%) were found to be in a similar range compared to other mesostructured perovskite solar cells reported in the literature employing solution-processed MBI absorber layers (max. 0.42%).[11]
In the case of the mixed-halide semiconductor, the addition of chloride does not have a positive effect on the PV performance (max. 0.18%). The stabilized power output under maximum power point tracking for 300 s (**Figure 17B**) starting from backward bias was 0.24% (MBI, after 434 days) and 0.13% (MBIC, after 701 days). However, MBIC-based solar cells exhibit a substantially higher FF up to 60% due to slightly lower series and substantially higher shunt resistance values. Furthermore, MBIC-based solar cells show a considerably reduced hysteresis effect compared to MBI-based devices.

Figure 17C shows long-term stability measurements of MBI- and MBIC-based solar cells during storage under inert conditions. The MBI-based solar cells reveal quite promising stability over the investigated period of time. Also, the MBIC-based devices showed over 100% of the initially measured PCE values even after about 700 days.

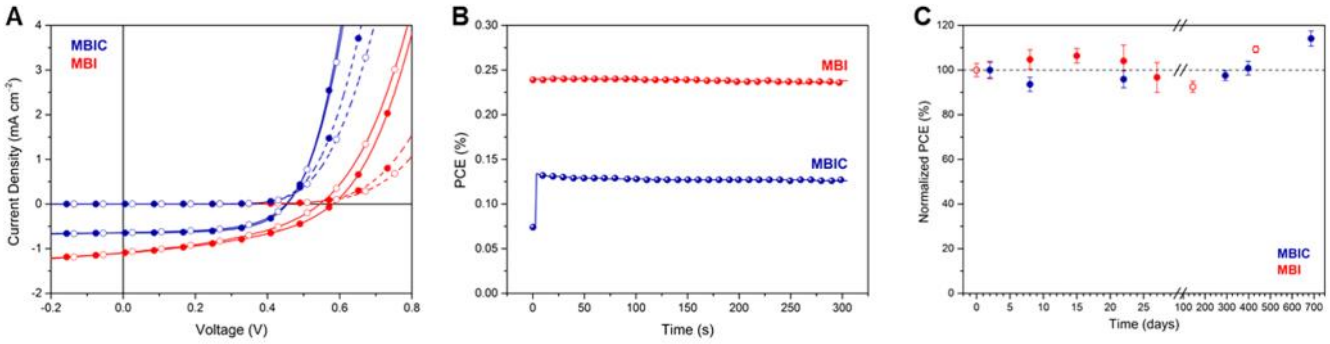

Figure 17. (A) J−V curves of mesoscopic solar cells employing MBIC and MBI absorbers measured in forward (empty symbols) and reverse (full symbols) scan directions, and (B) maximum power point tracking for 300 s. (C) Long-term stability test of solar cells with MBIC and MBI absorber layers under inert conditions. (Figure from [4])

3.5 Rubidium Antimony perovskites

[For more details see citation [12] and references therein]

Rubidium antimony halide perovskite single crystals ($Rb_3Sb_2Br_{9-x}I_x$) with different iodide/bromide ratios (denoted as PX-(9-x):x from PX-0-9 to PX-9-0 according to the Br/I ratio in the precursor solution) were prepared by a vapor diffusion crystallization technique with either dichloromethane or chloroform as anti-solvent from perovskite precursor solutions. All samples crystallized in the monoclinic space group P21 /n and cell parameters for $Rb_3Sb_2I_9$ (PX-0-9) and $Rb_3Sb_2Br_9$ (PX-9-0) prepared by the above stated protocol match literature data.[13] The lattice constants show a linear correlation as a function of the iodide content. The BX_6 octahedra size decreases with increasing bromide content (**Figure 18**). Also, the overall cell volume decreases (**Figure 18**).

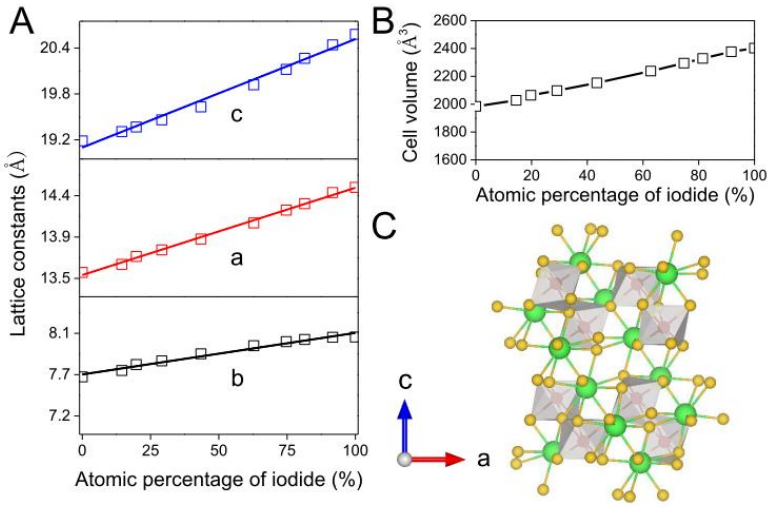

Figure 18. (A, B) Lattice constants and cell volume of $Rb_3Sb_2Br_{9-x}I_x$ plotted as a function of the iodide content, (C) crystal structure of Rb_3Sb2I_9 showing a 2D structure (red: Sb, green: Rb, yellow: I). (Figure from [12])

In a next step, thin films of the $Rb_3Sb_2Br_{9-x}I_x$ perovskites were deposited on glass using spin coating. The perovskite deposition was enhanced by a two-step anti-solvent treatment, already reported in literature. [14] XRD measurements of the perovskite thin films revealed a clear influence of the introduction of bromide into the perovskite crystal (**Figure 19**) that causes the unit cell to compress. In the XRD measurements, this is observable by the shift of the diffraction peaks to higher diffraction angles. Additionally, the diffraction patterns reveal that the preferential orientation of the perovskite crystallites is changing: while the $Rb_3Sb_2I_9$ thin film almost shows no preferential orientation and the measured pattern matches well with the reference pattern, the $Rb_3Sb_2Br_9$ layer crystallizes in a preferred orientation of the (001) plane parallel to the substrate surface indicated by the significantly increased intensity of the diffraction peaks at 18.5° and 27.0° 2□ corresponding to the (004) and (006) plane, respectively. No RbBr or RbI secondary phases were found in the XRD patterns of the thin film samples.

Using the Tauc-plot we determined an indirect band gap of 2.02 eV and a first direct transition of 2.24 eV. By substitution of $Rb_3Sb_2I_9$ towards $Rb_3Sb_2Br_9$, a blue shift of the absorption onset was observed. The absorption onset of the $Rb_3Sb_2Br_9$ film is approx. 460 nm and the Tauc plot reveals

an indirect band gap of 2.46 eV and a direct band transition of 2.76 eV. Similar to the lattice constants and the cell volume, also for the optical band gaps, a linear correlation with respect to the Br/I ratio is found. Moreover, an absorption spectrum of a $Rb_3Sb_2I_9$ perovskite thin film was measured after an ageing time of 18 h in ambient atmosphere. There was no visible change in absorption behavior, indicating a good stability of Sb-perovskite materials in ambient conditions.

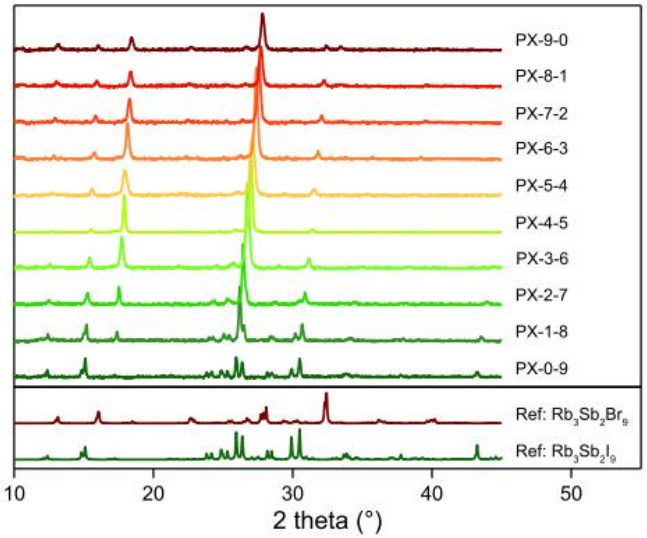

Figure 19. XRD patterns of $Rb_3Sb_2Br_{9-x}I_x$ perovskite thin films prepared on glass. The reference patterns were calculated based on the following data from the ICSD database: $Rb_3Sb_2I_9$: ICSD 243727; $Rb_3Sb_2Br_9$: ISCD 431322. (Figure from [12])

The film quality of the $Rb_3Sb_2Br_{9-x}I_x$ perovskites on glass/ITO/c-TiO_2/mp-TiO_2 substrates was investigated by scanning electron microscopy (SEM). Although an optimized deposition procedure adopted from Harikesh et al. [15] (including dripping with SbI_3/$SbBr_3$ dissolved in toluene) was used, the perovskites do not form a continuous overlayer on the mp-TiO_2 film and the homogeneity differs for every perovskite (**Figure 20**). Similar morphologies for antimony halide perovskite thin films have also been reported by other groups. [14,15] In this study, the perovskite sample PX-5-4 (**Figure 20F**) shows highest coverage of the mp-TiO_2 film. However, in this sample also larger voids are observed compared to the perovskite films of e.g. PX-0-9 to PX-3-6 (**Figure 20A-D**) and PX-7-2 (**Figure 20H**), which show similar homogeneity and grain size.

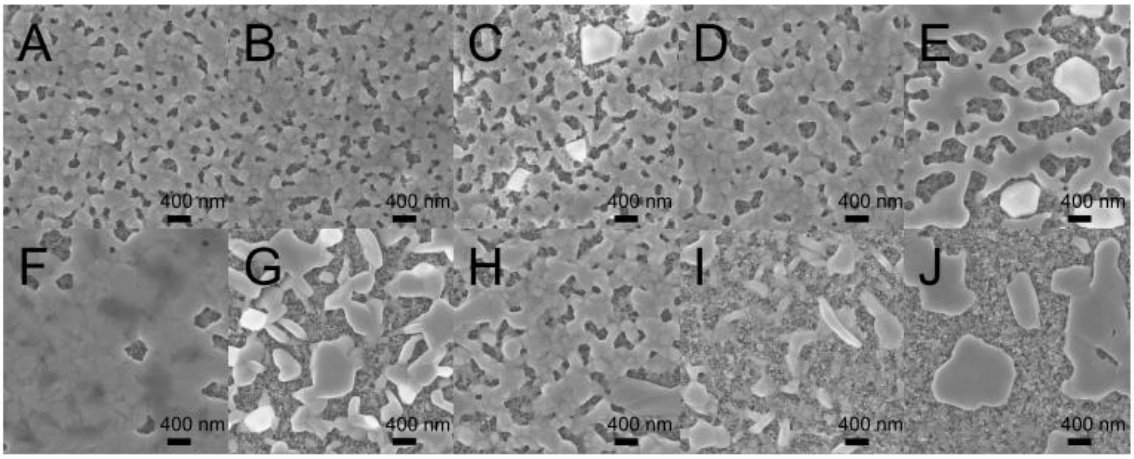

Figure 20. Top-view SEM images of $Rb_3Sb_2Br_{9-x}I_x$ films on mp-TiO_2 layers, PX-0-9 (A), PX-1-8 (B), PX-2-7 (C), PX-3-6 (D), PX-4-5 (E), PX-5-4 (F), PX-6-3 (G), PX-7-2 (H), PX-8-1 (I), PX-9-0 (J). (Figure from [12])

Solar cells were fabricated with a n-i-p architecture: glass/ITO/c-TiO_2/mp-TiO_2/$Rb_3Sb_2Br_{9-x}I_x$/spiro-OMeTAD/Au. The J-V curves of the best devices, measured after light soaking for 30 minutes, are shown in **Figure 21A**. A maximum PCE of 1.37% was reached for unmasked solar cells with $Rb_3Sb_2I_9$ (PX-0-9) as absorber showing a V_{OC} of 0.55 V, a J_{SC} of 4.25 mA/cm^2 and a FF of 59.5%. Using a shadow mask, the PCE was slightly reduced to a value of 1.11%, caused by a slightly reduced J_{SC}. The obtained PCEs for the solar cells with $Rb_3Sb_2I_9$ absorber layer are significantly higher than these reported up to now (~ 0.7%), [15,16] which is mainly based on a higher photocurrent. Based on the band gap of 2.03 eV of $Rb_3Sb_2I_9$ also a higher V_{OC} would seem feasible. However, the V_{OC} found here matches with the study by [15], in which the loss in V_{OC} was ascribed to defect levels in the perovskite absorber layer.

With increasing bromide content the PCE decreased to 0.01% for $Rb_3Sb_2Br_9$ (PX-9-0). Herein, the current density decreased with increasing bromide content, most likely due to a larger band gap for the bromide based compounds. In general, this should in turn increase the photovoltage, however, the photovoltage decreased. As discussed above, the increased intensity of the (006) reflection in the XRD-patterns with increasing bromide content revealed a stronger orientation of the a-b-planes, i.e. the connected SbI6-octaeder containing planes, parallel to the substrate, which is detrimental to an efficient charge transport.

The external quantum efficiency (EQE) spectra of the best performing $Rb_3Sb_2Br_{9-x}I_x$ based devices (PX-0-9 to PX-3-6) were measured and the spectra are depicted in **Figure 21C**. The PX-0-9 based solar cells display highest EQE values of 26.7%, whereas the solar cells based on PX-1-8, PX-2-7 and PX-3-6 absorber layers show maximum EQE values of 26.1%, 16.8% and 7.4%, respectively. The shapes of the EQE spectra are very similar to the absorption spectra of the corresponding perovskite films and the increased band gap of the perovskites with increasing Br-content is also reflected in the EQE spectra.

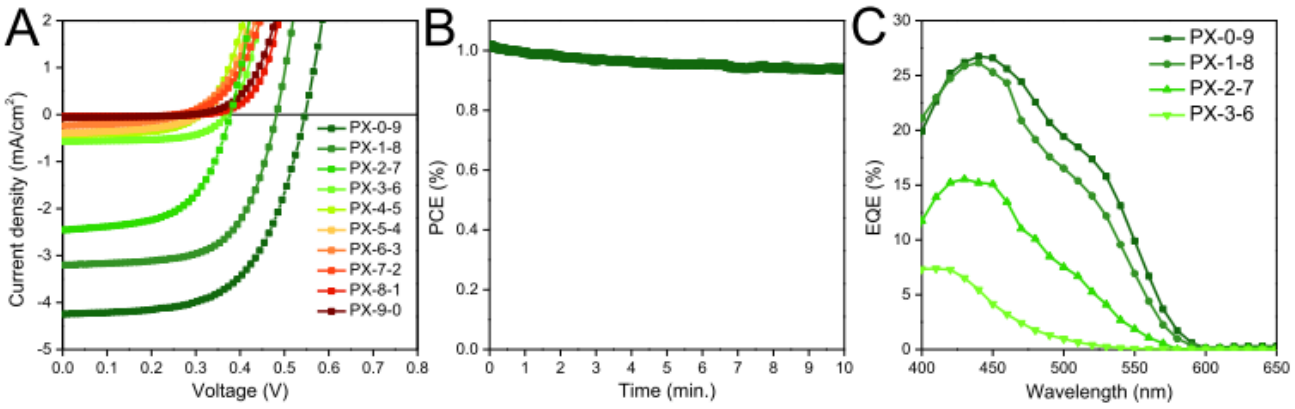

Figure 21. J-V curves of $Rb_3Sb_2Br_{9-x}I_x$-based solar cells measured in backward direction from 1000 mV to 0 mV with a scan rate of 100 mV/s (A), maximum power point tracking measurement of a Rb3Sb2I9 based solar cell (B), EQE spectra of the solar cells prepared with rubidium antimony halide perovskite layers with compositions from $Rb_3Sb_2I_9$ (PX-0-9) to PX-3-6 (C). (Figure from [12])

We further investigated the stability of the $Rb_3Sb_2I_9$-based devices under inert conditions (nitrogen atmosphere). The cells were stored in the glove box in the dark and measured periodically at an illumination of 100 mW/cm^2 . After more than 150 days of storage, the devices still exhibit 84% of their initial efficiency.

3.6 Tin perovskites

[For more details see citation [17] and references therein]

In our effort to develop a stable Sn-based perovskite, we combined an optimized double antisolvent dripping procedure using chlorobenzene in combination with a fast heating annealing step via putting the substrate directly after spin coating on a pre-heated hot plate for the annealing of the perovskite layer to obtain a homogeneous and pinhole free absorber layer. We used the MA-rich 2D/3D tin perovskite $MA_{0.75}FA_{0.15}PEA_{0.1}SnI_3$ as absorber material in this study (MA: methylammonium, FA: formamidinium, PEA: phenylethylammonium), as it shows a significantly lower band gap and extended photocurrent generation up to 1000 nm without severely reducing the photovoltage compared to higher band gap tin perovskites. Furthermore, we investigated the shelf lifetime as well as the stability of these devices under operation.
For the preparation of the perovskite absorber layer, the corresponding amounts of MAI, FAI, PEAI, and SnI_2, as well as 10 mol% SnF_2 as additive were dissolved in a mixture of dimethylformamide (DMF) and dimethyl sulfoxide (DMSO) to obtain the desired composition.

In a first step, the influence of antisolvent dripping and annealing conditions on the film morphology were investigated. Therefore, thin Sn perovskite films were prepared on glass/ITO substrates covered with a PEDOT:PSS layer. Many parameters influence the antisolvent dripping step, making this step one of the most critical in perovskite thin film processing. In our case, the basic procedure started by applying the antisolvent dripping step 20 s after starting the spinning process. Thereby, the distance between pipette tip and substrate was adjusted to approximately 4.5 cm. The layers were then put on a cold heating plate and heated up to 70 °C. The corresponding SEM images of the perovskite thin films prepared as described above are shown in **Figure 22A** and **D**. The single antisolvent dripping followed by slow heating led to large grain sizes (110–270 nm) accompanied by numerous pinholes. Putting the substrate on a pre-heated plate (70 °C) directly after spin coating resulted in a significantly reduced amount of pinholes and also a slightly decreased average grain size (80–230 nm), as can be seen in the SEM images in **Figure 22B** and **E**. By introducing a double anti-solvent dripping after 20 s and 80 s of the spin coating process combined with placing the substrates on a pre-heated hot plate (70 °C), the number of pinholes could be further diminished and also the grain size became slightly smaller (75–205 nm, see **Figure 22C** and **F**).

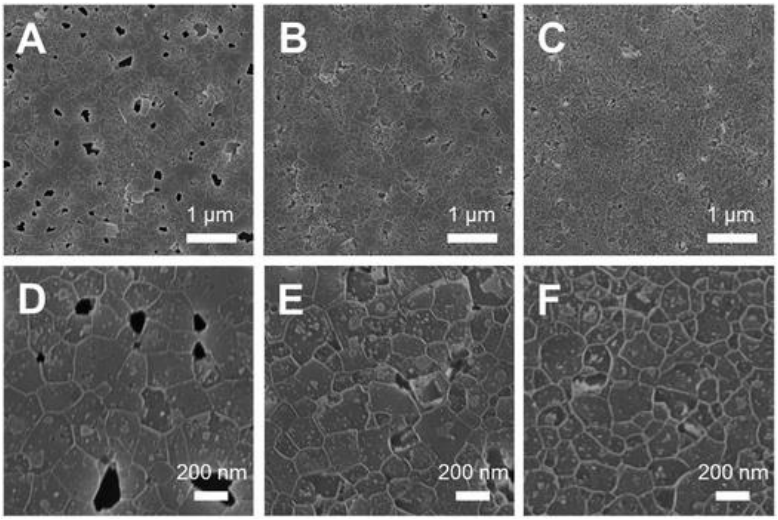

Figure 22. SEM images of tin perovskite thin films prepared by (A and D) a single antisolvent dripping after 20 s and slow heating to 70 °C, (B and E) a single antisolvent dripping after 20 s and directly placing the substrate on a 70 °C hot plate and (C and F) a double antisolvent dripping after 20 and 80 s and directly placing the substrate on a 70 °C hot plate. (Figure from [17])

The XRD of the $MA_{0.75}FA_{0.15}PEA_{0.1}SnI_3$ perovskite film prepared with the optimized processing conditions reveals a typical pattern for a mixed 2D/3D tin perovskite with quasi-cubic/orthorhombic crystal structure (see Figure 23). The 100 and 200 peaks at 14.1 and 28.5° 2θ are very pronounced in the diffractogram, indicating a preferred orientation of the (h00) planes of the perovskite crystals parallel to the substrate. The weak peaks at 43.4 and 59.0° 2θ can be most likely assigned to the 300 and 400 planes. Moreover, two minor peaks at 13.6 and 27.4° 2θ are present in the diffractogram. These are corresponding to slightly higher d values (6.51 and 3.25 Å) compared to the 100 and 200 peaks with d values of 6.28 and 3.13 Å, respectively. Thus, we assume that they can be correlated to a secondary phase exhibiting a slightly larger lattice spacing.

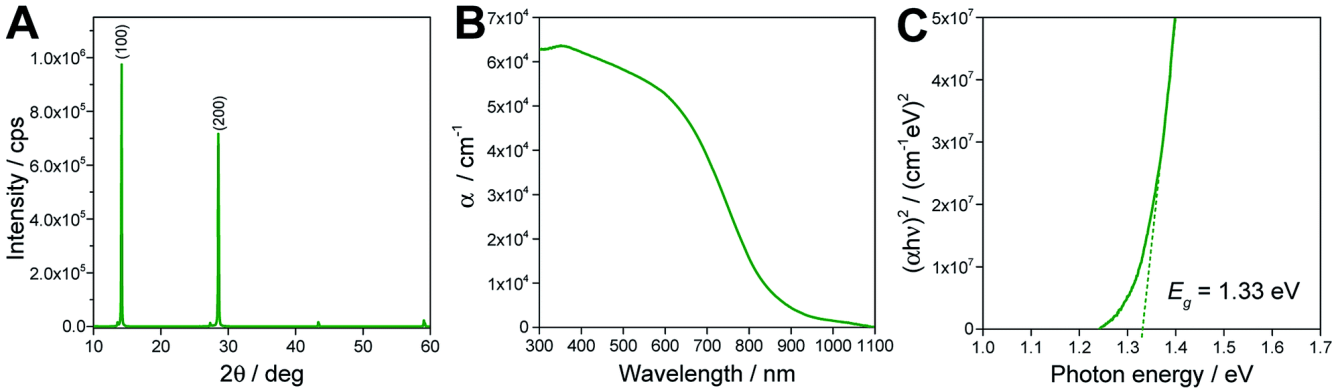

Figure 23. (A) X-ray diffraction pattern, (B) UV-Vis absorption spectrum and (C) Tauc plot of a $MA_{0.75}FA_{0.15}PEA_{0.1}SnI_3$ thin film on a glass substrate. (Figure from [17])

The UV-Vis absorption spectrum of the film is depicted in **Figure 23** and reveals an absorption onset at approx. 1000 nm. Via the corresponding Tauc plot, a direct band gap of 1.33 eV is determined. The low

band gap of this 2D/3D tin perovskite gives promise to obtain high photocurrents with this absorber material.

Next, we prepared solar cells with the optimized deposition conditions in the architecture glass/ITO/PEDOT:PSS/Sn-perovskite/$PC_{60}BM$/Al (**Figure 24**). The film thickness of the $MA_{0.75}FA_{0.15}PEA_{0.1}SnI_3$ absorber layers is around 225 nm. With this device setup, solar cells with PCEs up to 5.0% could be obtained in this study. The JV curves of a typical solar cell measured in forward direction are depicted in **Figure 24B**. The solar cell exhibits a J_{SC} of 18.4 mA cm^{-2}, a V_{OC} of 0.45 V and a FF of 0.61 leading to the PCE of 5.0%.

Compared to the solar cells with the triple cation tin perovskite absorbers, double cation perovskite-based devices with the compositions $MA_{0.9}PEA_{0.1}SnI_3$, $FA_{0.9}PEA_{0.1}SnI_3$, and $MA_{0.75}FA_{0.25}SnI_3$, prepared with the same anti-solvent dripping procedure, revealed lower PCEs. While solar cells with $MA_{0.9}PEA_{0.1}SnI_3$ absorber layers led to PCEs around 4.1%, the $FA_{0.9}PEA_{0.1}SnI_3$ based solar cells revealed PCEs of 1.6%. The devices prepared with $MA_{0.75}FA_{0.25}SnI_3$ perovskites only showed efficiencies of 0.4%.

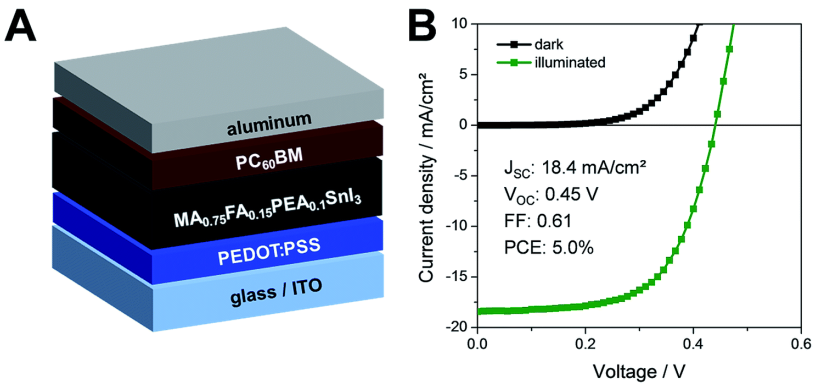

Figure 24. (A) Schematic of the used solar cell architecture, (B) JV curves of the tin perovskite solar cell with the highest PCE prepared within this study measured in forward scan direction 120 h after fabrication. (Figure from [17])

Moreover, the prepared solar cells show a stable shelf life over more than 5000 hours. In this shelf life test, the solar cell was stored in a N_2 filled glove box in ambient light conditions between the measurements. Up to 120 h after the fabrication we observed an increasing performance of the solar cells. The V_{OC} and FF show a very stable behaviour over time. The biggest changes are observed in the J_{SC}, which increases up to 120 h after the fabrication of the solar cell. In the further course of the test, the J_{SC} ranges between 85 and 100% of the maximum value. At the end of the testing period, after 5424 h, the solar cell has still a PCE of 4.7% which corresponds to 87% of the highest performance of this solar cell.

Due to the exceptional shelf life of these tin perovskite solar cells in inert conditions, we performed a further stability test under active load at maximum power point conditions and continuous illumination in inert atmosphere to simulate conditions which are near to real operation conditions of encapsulated

photovoltaic devices. As can be seen in **Figure 25**, over the period of the test of 72 hours (in particular in the first hours), the J_{MPP} as well as the V_{MPP} slightly increased which results not only in a stable behavior of the solar cell but even in a slight enhancement of the PCE from 3.5 to 4.1% during the continuous operation of the solar cell over 72 hours. We assume that the very limited trap-assisted recombination in these devices is a major pillar for the good shelf life and, in particular, also for the stable performance under continuous illumination and active load.

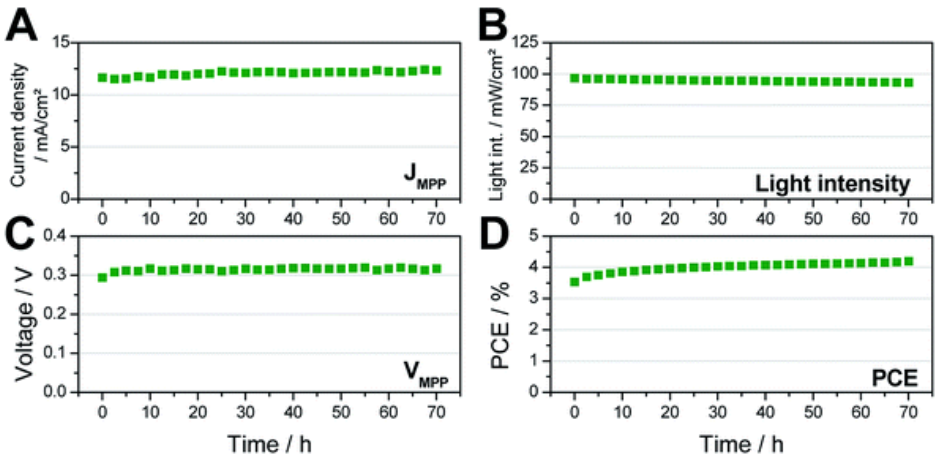

Figure 25. Results of a stability test performed in nitrogen atmosphere under continuous illumination and active load at the maximum power point; (A) J_{MPP}, (B) light intensity, (C) V_{MPP}, (D) PCE. Every 150th data point is shown. (Figure from [17])

With the target to further explore the environmental stability of the Sn-based perovskites, we have followed two further approaches. The first was to incorporate copper into the tin perovskite, thus obtained a Sn-Cu mixed perovskite material. The second approach was to form the Sn-perovskite absorber and then cap the absorber with a 2D Cu perovskite film. The 2D Cu perovskite has an exceptional environmental stability and we anticipated that this material will protect the underlying Sn-perovskite. The two approaches can be seen in **Figure 26**.

For the $MA_{0.75}FA_{0.15}PEA_{0.10}SnI_3$ perovskite the solution components are: DMSO:DMF as solvent; methyl-ammonium Iodide (MAI); Formamidinium Iodide (FAI); Phenylethylammonium Iodide (PEAI); Tin Iodide (SnI_2), Tin Fluoride (SnF_2). For the mixed Sn-Cu perovskite the components are: DMSO:DMF; MAI; FAI); PEAI; SnI_2, $CuBr_2$, SnI_2.

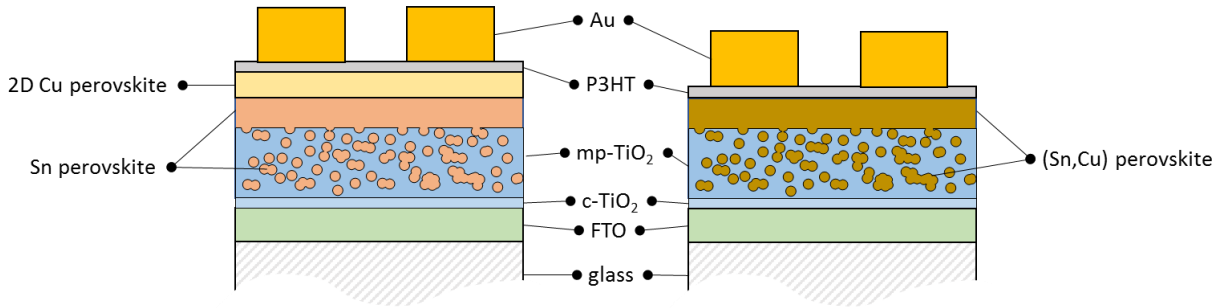

Figure 26 Schematic of the solar cell architectures with the Sn perovskite capped with 2D Cu perovskite and with the mixed (tin, copper) absorber.

In **Figure 27** we can see cross section SEM images of the cells with the Sn perovskite absorber capped with the 2D Cu perovskite.

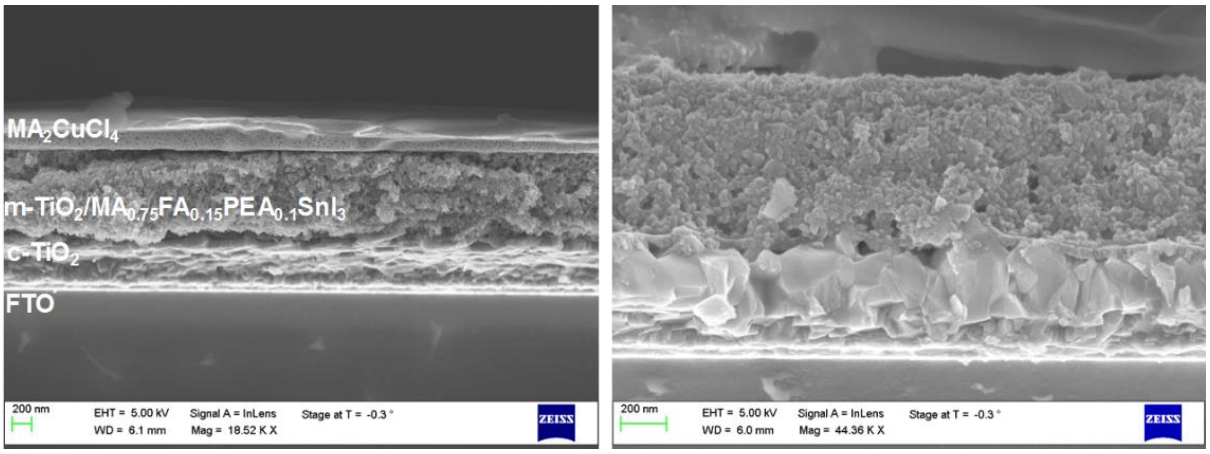

Figure 27 Cross section SEM images of the solar cell with the Sn perovskite capped with 2D Cu perovskite.

In **Figure 28** we show the PV performance for best cells with the two architectures. Mean efficiency values for architecture 1 and 2 are n=3.04 ± 0.95 % and n=1.65 ± 0.4 %, respectively. The cells were measured without encapsulation in ambient environment. Cells without the Cu perovskite capping or cells with the pure Sn perovskite absorber was not possible to be measured in ambient conditions without encapsulation.

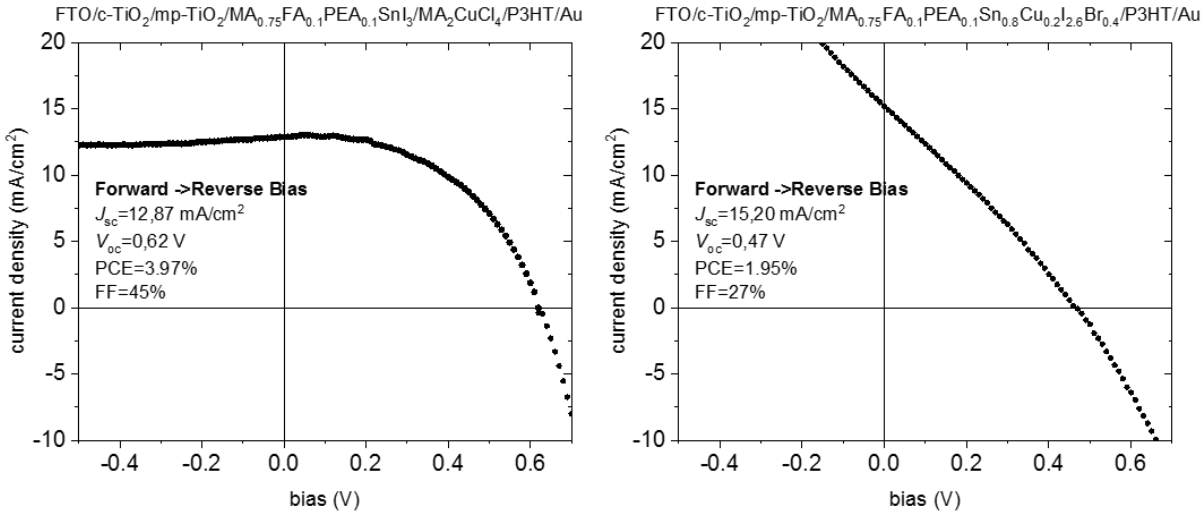

Figure 28. J-V characteristics of the solar cells with the Sn perovskite absorbers.

4 Conclusions

In the sections above, we have elaborated on the content of the project, related to the most important tasks that were to investigate Pb-free perovskite absorber materials from the theoretical and experimental perspective. The most important results and conclusions are the following:

- A multitude of Pb-free perovskites could be identified by theoretical band structure calculations as potential candidates for use as solar cell absorbers, on the basis of their bandgap. Some of these prominent candidates are based on tin, zinc, cadmium, germanium, bismuth and others, with a bandgap between 1 and 2.5 eV. Many other compounds, such as compounds based on Barium or Strontium are predicted to have too large bandgap for solar cell applications. Apart from the 3-dimensional compounds, some promising candidates have lower dimensionality, such as the Bi-based perovskites. Lower dimensionality is in many case related to better environmental stability, which is a very important asset for solar cell implementation.
- We could show considerable photovoltaic performance in solar cells with methylammonium germanium mixed Cl/Br halide perovskites. Solar cells with the $MAGeI_{2.7}Br_{0.3}$ absorber layer, processed at low temperature with PEDOT:PSS and PCBM as hole and electron transport layers respectively, showed power conversion efficiency of 0.57%. Even though the step forward in power conversion efficiency with this material is encouraging, the stability of the devices is very limited and remains a crucial issue.
- 2D Copper-based methylammonium mixed Cl/Br perovskites present suitable bandgaps for use as PV absorber (some below 2 eV) and they have also shown very high environmental stability, attributed to their 2D structure. On the other hand, their implementation in solar cells did not lead to a measurable PV efficiency. Despite this, Cu can be combined with other cations (like Sn) in perovskite compounds to enhance their stability.
- Partial exchange of iodide to chloride ions in the methylammonium bismuth iodide perovskite (MBI) led to the new A_6BX_9-type mixed-anion halogenobismuthate(III) semiconductor $MA_6BiI_{5.22}Cl_{3.78}$ (MBIC) exhibiting a significantly different crystal structure compared to the pure iodide compound. The optoelectronic properties of this new material are quite similar to those of MBI. The experimentally found optical band gap of 2.25 eV is in good agreement with the calculated value of 2.50 eV derived from DFT simulations. Transient photoluminescence measurements reveal that the PL decay times are significantly reduced in MBIC/mp-TiO_2 heterojunctions compared to MBIC films on glass, indicating an efficient electron transfer from MBIC to TiO_2. Solar cells with MBIC absorber fabricated with mp-TiO_2 and spiro-OMeTAD as electron and hole transport layer, respectively, showed PCE values up to 0.18%, enhanced FF values, and a suppressed hysteretic behavior. When stored under inert conditions, these solar cells show an excellent long-term stability over the investigated period of more than 700 days.
- Rubidium Antimony halide perovskites, of monoclinic structure, were successfully fabricated and tested in solar cells. Increasing bromide content compresses the BX6 octahedron, thus reducing the perovskite volume from $Rb_3Sb_2I_9$ to $Rb_3Sb_2Br_9$. The single crystals reveal a layered structure for all perovskites. In thin films, $Rb_3Sb_2I_9$ shows no preferential orientation. However, increasing the bromide content in the perovskite led to preferential growth alongside the (001) plane. When

they are implemented in a n-i-p solar cell structure using TiO_2 as electron transport layer and spiro-OMeTAD as hole transport layer, a maximum PCE of 1.37% for devices using the perovskite $Rb_3Sb_2I_9$ was recorded. With increasing bromide content, the device efficiency decreased significantly. $Rb_3Sb_2I_9$-based solar cells feature good stability, after more than 150 days still approx. 85% of the initial PCE are retained.

- Multiple organic cation Sn perovskites with increased stability were fabricated, showing also enhanced PV performance. It could be shown that the amount of pinholes in the $MA_{0.75}FA_{0.15}PEA_{0.1}SnI_3$ perovskite layer can be significantly reduced by a double antisolvent dripping procedure. The solar cells with these absorber layers revealed PCEs up to 5.0%, showing only minor trap-4assisted recombination. In the shelf life test, the solar cell performance only diminished marginally from 5.0 to 4.7% after more than 5400 hours. The stability test under active load and continuous illumination even revealed a slight increase of the PCE during a period of more than 70 h. The time spans of the herein presented stability data are among the longest reported for tin perovskite-based solar cells so far and the observed results are very encouraging. In future work, we will conduct further stability tests under various testing conditions to gain more information about the stability of tin perovskite solar cells. Moreover, the impact of the optimized anti-solvent and annealing procedure on charge carrier densities in the perovskite, which is a further key to improving the performance as well as the stability of this absorber, is currently under investigation.

5 Outlook

Perovskite solar cells are still the most fascinating class of new solar cell materials and estimated 10.000 researchers worldwide are working on lead-based, as well as lead-free materials. Whereas Pb-based materials show PCE values of more than 24% in laboratory solar cell devices, also lead-free devices have made fast progress. Tin perovskite-based materials are now reaching almost 10% and the research on lead-free materials has now accelerated worldwide.

PERMASOL allowed the consortium to participate in this forefront research and it was possible to obtain valuable results published in renowned scientific journals and recognized by the international scientific community. For the consortium partners this project was a nucleus for a new research topic, which will be continued in the future. We are currently preparing several following-up research proposals in basic but also in applied research proposals.

6 Literature

[1] A. Koliogiorgos, S. Baskoutas, I. Galanakis, Electronic and gap properties of lead-free perfect and mixed hybrid halide perovskites: An ab-initio study, Comput. Mater. Sci. 138 (2017) 92–98. doi:10.1016/j.commatsci.2017.06.026.

[2] G. Moschou, A. Koliogiorgos, I. Galanakis, Electronic Properties of Cs-Based Halide Perovskites: An Ab Initio Study, Phys. Status Solidi A. 215 (2018) 1700941. doi:10.1002/pssa.201700941.

[3] A. Koliogiorgos, S. Baskoutas, I. Galanakis, Electronic and gap properties of Sb and Bi based halide perovskites: An ab-initio study, Comput. Condens. Matter. 14 (2018) 161–166. doi:10.1016/j.cocom.2018.02.001.

[4] S.F. Hoefler, T. Rath, R. Fischer, C. Latal, D. Hippler, A. Koliogiorgos, I. Galanakis, A. Bruno, A. Fian, T. Dimopoulos, G. Trimmel, A Zero-Dimensional Mixed-Anion Hybrid Halogenobismuthate(III) Semiconductor: Structural, Optical, and Photovoltaic Properties, Inorg. Chem. 57 (2018) 10576–10586. doi:10.1021/acs.inorgchem.8b01161.
[5] G.E. Eperon, G.M. Paternò, R.J. Sutton, A. Zampetti, A.A. Haghighirad, F. Cacialli, H.J. Snaith, Inorganic caesium lead iodide perovskite solar cells, J. Mater. Chem. A. 3 (2015) 19688–19695. doi:10.1039/C5TA06398A.
[6] I. Kopacic, B. Friesenbichler, S.F. Hoefler, B. Kunert, H. Plank, T. Rath, G. Trimmel, Enhanced Performance of Germanium Halide Perovskite Solar Cells through Compositional Engineering, ACS Appl. Energy Mater. (2018). doi:10.1021/acsaem.8b00007.
[7] T. Krishnamoorthy, H. Ding, C. Yan, W.L. Leong, T. Baikie, Z. Zhang, M. Sherburne, S. Li, M. Asta, N. Mathews, S.G. Mhaisalkar, Lead-free germanium iodide perovskite materials for photovoltaic applications, J. Mater. Chem. A. 3 (2015) 23829–23832. doi:10.1039/C5TA05741H.
[8] J. Qian, B. Xu, W. Tian, A comprehensive theoretical study of halide perovskites ABX 3, Org. Electron. 37 (2016) 61–73. doi:10.1016/j.orgel.2016.05.046.
[9] C.C. Stoumpos, L. Frazer, D.J. Clark, Y.S. Kim, S.H. Rhim, A.J. Freeman, J.B. Ketterson, J.I. Jang, M.G. Kanatzidis, Hybrid Germanium Iodide Perovskite Semiconductors: Active Lone Pairs, Structural Distortions, Direct and Indirect Energy Gaps, and Strong Nonlinear Optical Properties, J. Am. Chem. Soc. 137 (2015) 6804–6819. doi:10.1021/jacs.5b01025.
[10] D. Cortecchia, H.A. Dewi, J. Yin, A. Bruno, S. Chen, T. Baikie, P.P. Boix, M. Grätzel, S. Mhaisalkar, C. Soci, N. Mathews, Lead-Free MA2CuClxBr4–x Hybrid Perovskites, Inorg. Chem. 55 (2016) 1044–1052. doi:10.1021/acs.inorgchem.5b01896.
[11] X. Zhang, G. Wu, Z. Gu, B. Guo, W. Liu, S. Yang, T. Ye, C. Chen, W. Tu, H. Chen, Active-layer evolution and efficiency improvement of (CH3NH3 3Bi2I9-based solar cell on TiO2-deposited ITO substrate, Nano Res. 9 (2016) 2921–2930. doi:10.1007/s12274-016-1177-8.
[12] S. Weber, T. Rath, K. Fellner, R. Fischer, R. Resel, B. Kunert, T. Dimopoulos, A. Steinegger, G. Trimmel, Influence of the Iodide to Bromide Ratio on Crystallographic and Optoelectronic Properties of Rubidium Antimony Halide Perovskites, ACS Appl. Energy Mater. 2 (2019) 539–547. doi:10.1021/acsaem.8b01572.
[13] J.-H. Chang, T. Doert, M. Ruck, Structural Variety of Defect Perovskite Variants M3E2X9 (M= Rb, Tl, E= Bi, Sb, X= Br, I): Structural Variety of Defect Perovskite, Z. Für Anorg. Allg. Chem. 642 (2016) 736–748. doi:10.1002/zaac.201600179.
[14] J.-C. Hebig, I. Kühn, J. Flohre, T. Kirchartz, Optoelectronic Properties of (CH3NH3)3Sb2I9 Thin Films for Photovoltaic Applications, ACS Energy Lett. 1 (2016) 309–314. doi:10.1021/acsenergylett.6b00170.
[15] P.C. Harikesh, H.K. Mulmudi, B. Ghosh, T.W. Goh, Y.T. Teng, K. Thirumal, M. Lockrey, K. Weber, T.M. Koh, S. Li, S. Mhaisalkar, N. Mathews, Rb as an Alternative Cation for Templating Inorganic Lead-Free Perovskites for Solution Processed Photovoltaics, Chem. Mater. 28 (2016) 7496–7504. doi:10.1021/acs.chemmater.6b03310.
[16] J.-P. Correa-Baena, L. Nienhaus, R.C. Kurchin, S.S. Shin, S. Wieghold, N.T. Putri Hartono, M. Layurova, N.D. Klein, J.R. Poindexter, A. Polizzotti, S. Sun, M.G. Bawendi, T. Buonassisi, A-Site Cation in Inorganic A3Sb2I9 Perovskite Influences Structural Dimensionality, Exciton Binding Energy, and Solar Cell Performance, Chem. Mater. 30 (2018) 3734–3742. doi:10.1021/acs.chemmater.8b00676.
[17] T. Rath, J. Handl, S. Weber, B. Friesenbichler, P. Fürk, L. Troi, T. Dimopoulos, B. Kunert, R. Resel, G. Trimmel, Photovoltaic properties of a triple cation methylammonium/formamidinium/phenylethylammonium tin iodide perovskite, J. Mater. Chem. A. 7 (2019) 9523–9529. doi:10.1039/C9TA02835H.

7 Contact

Dr. Theodoros Dimopoulos
AIT Austrian Institute of Technology, Giefinggasse 4, 1210 Vienna,
Tel: 050 550 6201
www.ait.ac.at

Dr. Gregor Trimmel
Graz University of Technology, Institute for Chemistry and Technology of Materials
https://ictm.tugraz.at

Dr. Bernhard Lamprecht
Joanneum Research, Materials
www.joanneum.at